Radiation as the dominant cause of Temperature Extremes on the Tibetan Plateau

Tian Yinglin[1], Ghausi Sarosh Alam[2], Zhang Yu[1], Zhong Deyu[1], Wang G. Q.[1], and Kleidon Axel[3]

[1]Tsinghua University
[2]Indian Institute of Technology Bombay
[3]Max-Planck-Institute for Biogeochemistry

November 16, 2022

Abstract

Temperature extremes have been related to anomalies in the large-scale circulation, but how these alter the surface energy balance is less clear. Here, we attributed extremes in daytime and nighttime temperatures of the eastern Tibetan Plateau to anomalies in the surface energy balance. We find that daytime temperature extremes are mainly caused by altered solar radiation, while nighttime extremes are controlled by changes in dowelling longwave radiation. These radiation changes are largely controlled by cloud variations, which are further associated with certain large-scale circulations through modulating vertical air motion and horizontal cloud convergence. Anomalies in heat advection, soil moisture, and snow albedo played secondary roles in triggering the initial change and contributed mostly to maintaining the duration. These mechanisms are consistent during winter and summer, also holding for cold extremes. Our work implies more frequent and severe warm nights and compound warm events over the Tibetan Plateau in the future.

Yinglin Tian[1], Sarosh Alam Ghausi[2], Deyu Zhong[1], Yu Zhang[1], Guangqian Wang[1], and Axel Kleidon[2]

[1]State Key Laboratory of Hydroscience and Engineering, Department of Hydraulic Engineering, Tsinghua University, 100084 Beijing, China

[2]Biospheric Theory and Modelling, Max Planck Institute for Biogeochemistry, 07701 Jena, Germany

Corresponding author:

Axel Kleidon (*akleidon@bgc-jena.mpg.de*), Deyu Zhong (zhongdy@tsinghua.edu.cn)

Table S1 . Characteristics of extremely warm events during winter

	Daytime	Daytime	Daytime	Daytime	Daytime	Nighttime	Nighttime	Nighttime	Nighttime
Single warm day threshold	3.89 K (176 d)	3.89 K (176 d)	3.89 K (176 d)	3.89 K (176 d)	3.89 K (176 d)	3.48 K (176 d)	3.48 K (176 d)	3.48 K (176 d)	3.48 K (176 d)
Lasting day(s)	1	2	3	>=4	Sumdays	1	2	3	>=4
warm events	43	29	15	5	170	105	27	3	0

	Daytime	Daytime	Daytime	Daytime	Daytime	Nighttime	Nighttime	Nighttime	Nighttime
Independent warm events	23	11	6	1	67	74	8	1	0
Compound warm events	17	17	9	4	98				
Others	3	1	0	0	5				

Table S2 . Characteristics of extremely warm events during summer

	Daytime	Daytime	Daytime	Daytime	Daytime	Nighttime	Nighttime	Nighttime	Nighttime
Single Warm day threshold	2.83 K (180 d)	2.83 K (180 d)	2.83 K (180 d)	2.83 K (180 d)	2.83 K (180 d)	2.23 K (180 d)	2.23 K (180 d)	2.23 K (180 d)	2.23 K (180 d)
Lasting day(s)	1	2	3	>=4	Sumdays	1	2	3	>=4
Warm events	50	25	10	10	178	41	22	7	15
Independent warm events	41	15	9	7	133	30	15	5	12
Compound warm events	7	7	0	3	34				
Others	2	3	1	0	11				

Table S3 . Characteristics of extremely cold events during winter

	Daytime	Daytime	Daytime	Daytime	Daytime	Nighttime	Nighttime	Nighttime	Nighttime
Single Cold day threshold	-4.01 K (176 d)	-4.01 K (176 d)	-4.01 K (176 d)	-4.01 K (176 d)	-4.01 K (176 d)	-3.34 K (176 d)	-3.34 K (176 d)	-3.34 K (176 d)	-3.34 K (176 d)
Lasting day(s)	1	2	3	>=4	Sumdays	1	2	3	>=4
Cold events	38	32	12	7	174	76	22	7	6
Independent Cold events	19	12	3	1	56	46	6	0	2
Compound Cold events	17	20	9	6	116				
Others	2	0	0	0	2				

Table S4 . Characteristics of extremely cold events during summer

	Daytime	Daytime	Daytime	Daytime	Daytime	Nighttime	Nighttime	Nighttime	Nighttime
Single Cold day threshold	-2.85 K (180 d)	-2.85 K (180 d)	-2.85 K (180 d)	-2.85 K (180 d)	-2.85 K (180 d)	-2.60 K (180 d)	-2.60 K (180 d)	-2.60 K (180 d)	-2.60 K (180 d)
Lasting day(s)	1	2	3	>=4	Sumdays	1	2	3	>=4
Cold events	58	35	11	3	175	53	30	13	4
Independent Cold events	46	17	6	1	102	37	16	9	1
Compound Cold events	9	18	5	2	70				
Others	3	0		0	3				

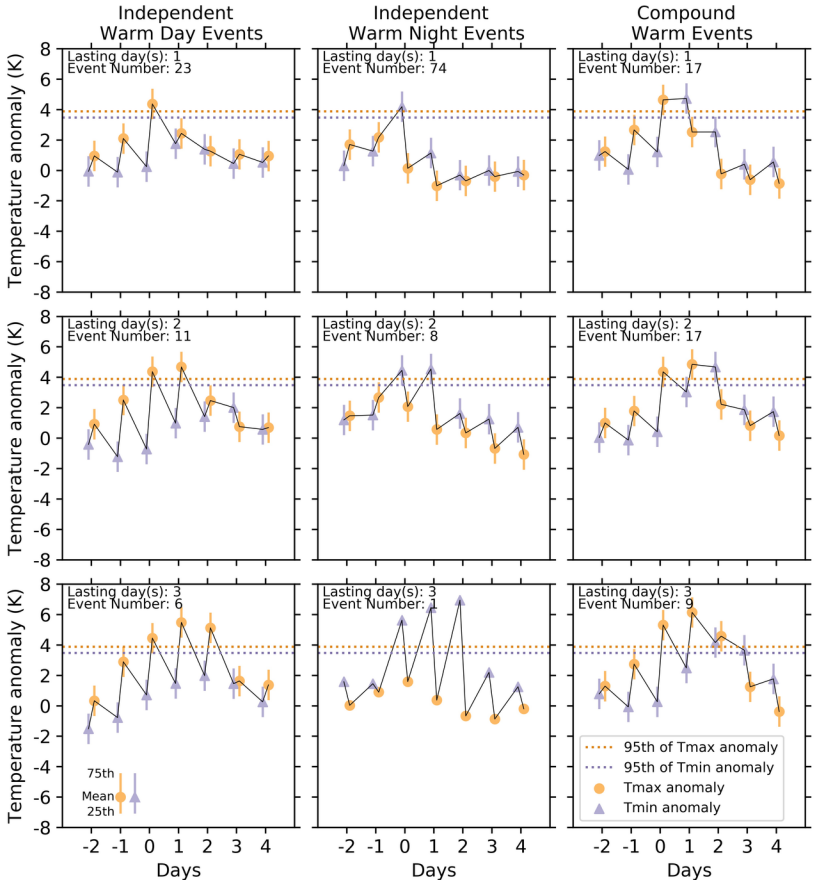

Figure S1 . Temperature anomaly evolution of independent warm day events (the first column), independent warm night events (the second column), and the compound warm events (the third column) during winter

lasting for 1, 2, and 3 days (the first, second, and the third rows).

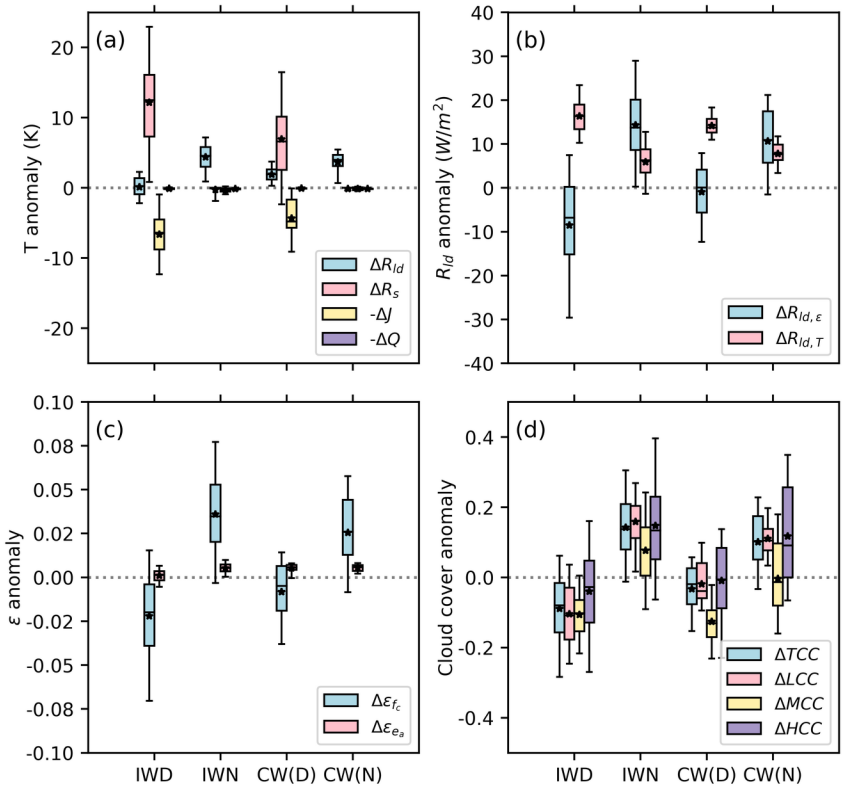

Figure S2. The same as Figure 2 but for warm events during summer

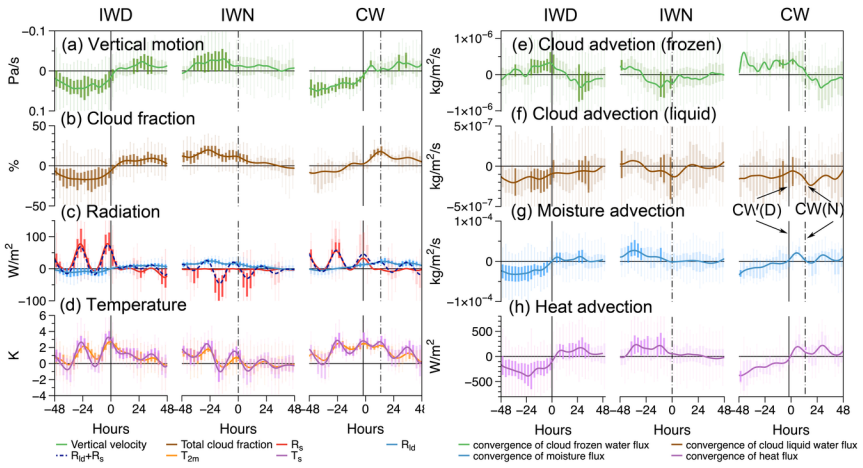

Figure S3. The same as Figure 3 but for warm events during summer

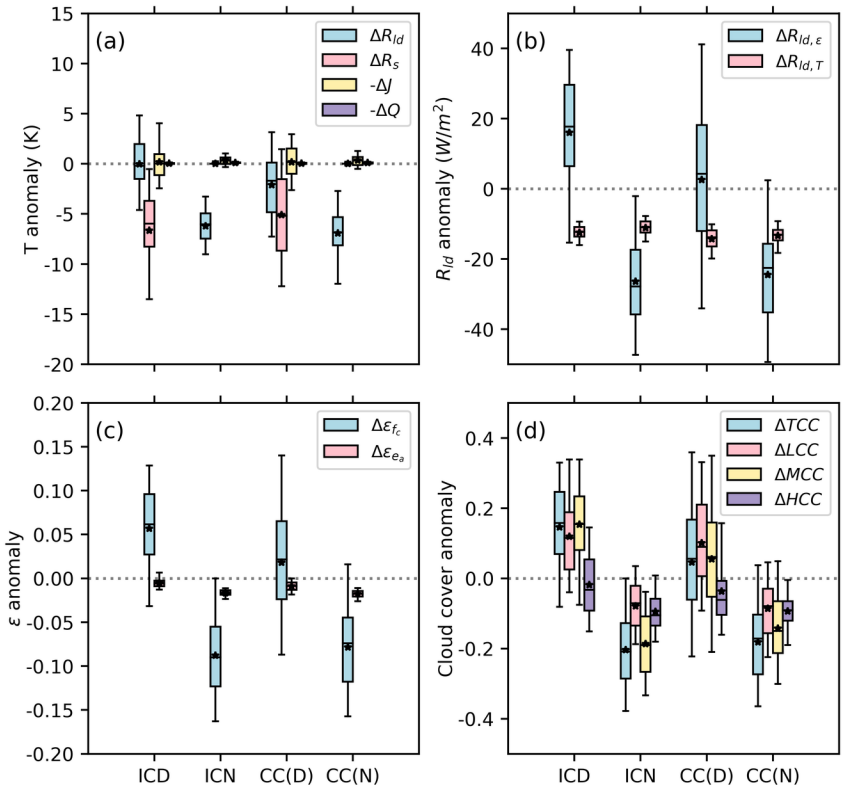

Figure S4. The same as Figure 2 but for independent cold day events (ICD), independent cold night events (ICN), and the compound cold events (CC, CCD: days, CCN: nights) during winter lasting for 1 day.

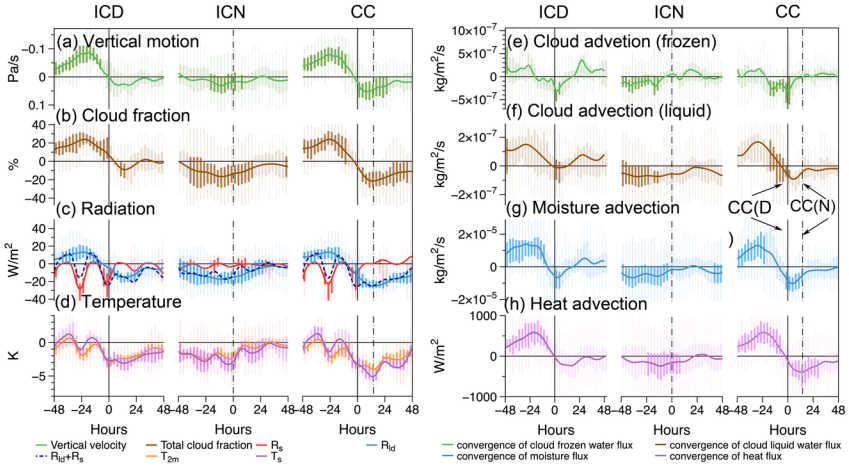

Figure S5. The same as Figure 3 but for independent cold day events (ICD), independent cold night events (ICN), and the compound cold events (CC, CCD: days, CCN: nights) during winter lasting for 1 day.

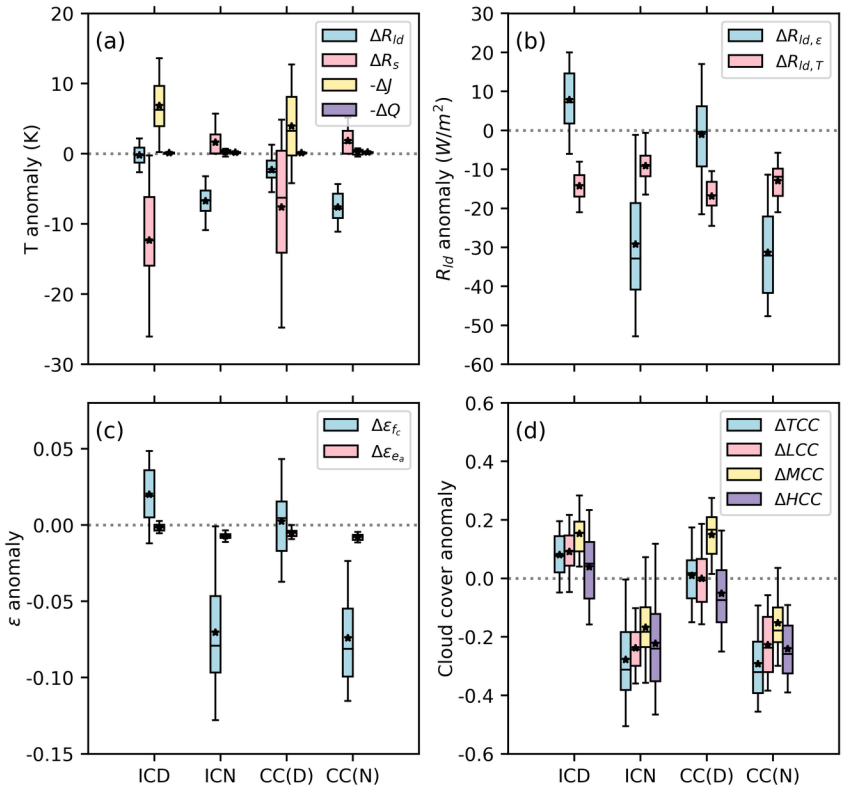

Figure S6. The same as Figure 2 but for independent cold day events (ICD), independent cold night events (ICN), and the compound cold events (CC, CCD: days, CCN: nights) during summer lasting for 1 day.

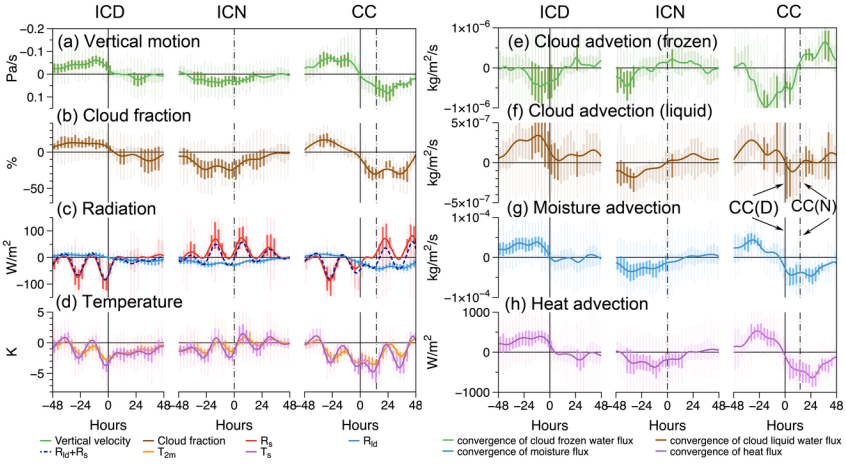

Figure S7. The same as Figure 3 but for independent cold day events (ICD), independent cold night events (ICN), and the compound cold events (CC, CCD: days, CCN: nights) during summer lasting for 1 day.

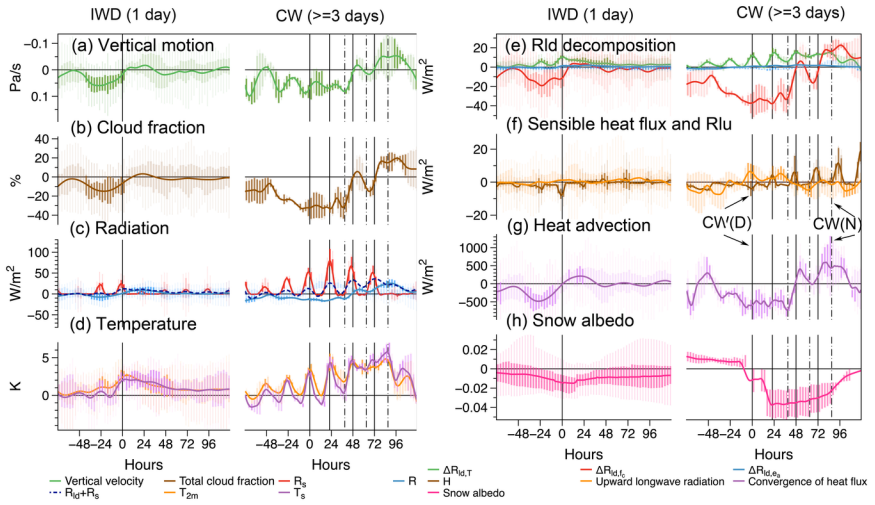

Figure S8. Anomaly evolution of (a) vertical velocity (downward positive), (b) cloud cover fraction, (c) shortwave and longwave radiation, (d) surface and air temperature, (e) contribution of cloud variation and air temperature (R_{ld,f_c} and $R_{ld,T}$) to downward longwave radiation, (f) surface sensible heat flux (H) and upward longwave radiation, (g) heat advection (vertically integrated convergence of temperature flux), and (h) snow albedo for independent warm day events (IWD) lasting for 1 day and compound warm events (CW, CWD: days, CWN: nights) lasting at least 3 days during the winter season. Vertical solid and dashed lines are extremely warm day and night, respectively. The box plot shows the mean value and ranges among events, with the upper and lower whistles presenting 95^{th} and 5^{th}, the upper and lower edge of the box presenting 75^{th} and 25^{th}. Heavy lines are Loess fit lines. Heavy color boxes present the value with statistical significance at the 95% confidence level based on a two-sample student's t-test.

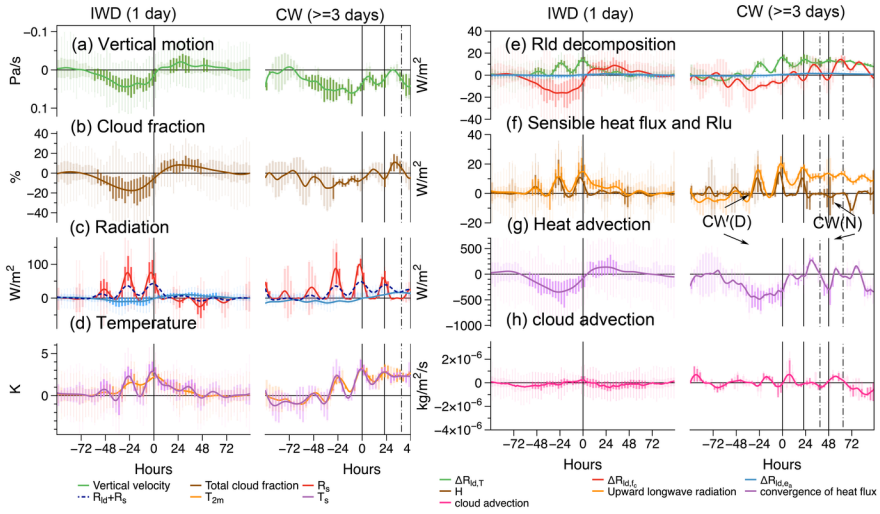

Figure S9. Anomaly evolution of (a) vertical velocity (downward positive), (b) cloud cover fraction, (c) shortwave and longwave radiation, (d) the surface and air temperature, (e) contribution of cloud variation and air temperature (R_{ld,f_c} and$R_{ld,T}$) to downward longwave radiation, (f) surface sensible heat flux (H) and

upward longwave radiation, (g) heat advection (vertically integrated convergence of temperature flux), and (h) cloud advection (vertically integrated convergence of cloud water flux, the fourth row) for independent warm day events (IWD) lasting for 1 day and compound warm events (CW, CWD: days, CWN: nights) lasting at least 3 days during the summer season. Vertical solid and dashed lines are extremely warm day and night, respectively. The box plot shows the mean value and ranges among events, with the upper and lower whistles presenting 95^{th} and 5^{th}, the upper and lower edge of the box presenting 75^{th} and 25^{th}. Heavy lines are Loess fit lines. Heavy color boxes present the value with statistical significance at the 95% confidence level based on a two-sample student's t-test.

Hosted file

`essoar.10512004.1.docx` available at https://authorea.com/users/524794/articles/595558-radiation-as-the-dominant-cause-of-temperature-extremes-on-the-tibetan-plateau

Yinglin Tian[1], Sarosh Alam Ghausi[2], Deyu Zhong[1], Yu Zhang[1], Guangqian Wang[1], and Axel Kleidon[2]

[1]State Key Laboratory of Hydroscience and Engineering, Department of Hydraulic Engineering, Tsinghua University, 100084 Beijing, China

[2]Biospheric Theory and Modelling, Max Planck Institute for Biogeochemistry, 07701 Jena, Germany

Corresponding author:

Axel Kleidon (akleidon@bgc-jena.mpg.de), Deyu Zhong (zhongdy@tsinghua.edu.cn)

Key Points:

- Daytime temperature extremes are directly shaped by anomalies of surface net solar radiation while nighttime extremes by variations in downward longwave radiation.
- Surface radiation anomalies are largely caused by cloud cover changes due to anomalies in the large-scale atmospheric circulation.
- Heat advection, surface sensible heat flux, and albedo variations appear to play secondary roles in amplifying the initial change but contribute to maintaining the temperature extremes.

Abstract

Temperature extremes have been related to anomalies in the large-scale circulation, but how these alter the surface energy balance is less clear. Here, we attributed extremes in daytime and nighttime temperatures of the eastern Tibetan Plateau to anomalies in the surface energy balance. We find that daytime temperature extremes are mainly caused by altered solar radiation, while nighttime extremes are controlled by changes in dowelling longwave radiation. These radiation changes are largely controlled by cloud variations, which are further associated with certain large-scale circulations through modulating vertical air motion and horizontal cloud convergence. Anomalies in heat advection, soil moisture, and snow albedo played secondary roles in triggering the initial change and contributed mostly to maintaining the duration. These mechanisms are consistent during winter and summer, also holding for cold extremes. Our work implies more frequent and severe warm nights and compound warm events over the Tibetan Plateau in the future.

Plain Language Summary

The Tibetan Plateau has witnessed a substantial increase in warm days and nights, leading to a more vulnerable ecosystem and making it more important to identify the underlying physical causes. The extremely warm events have been previously found to be accompanied by anomalies in large-scale circulation, which seems to be associated with horizontal heat advection at the first sight. However, in this paper, based on surface energy balance, we showed that warm days and nights in the eastern Tibetan plateau are dominated by net

solar radiation and downward longwave radiation, respectively. Moreover, radiation is largely influenced by cloud changes associated with synoptic climate settings, i.e., low pressure favors air ascent, which enhances condensation and cloud formation, while high pressure is on the contrary. This mechanism is generally consistent for both summer and winter seasons, and also warm and cold extremes. Other factors, e.g., anomalies in heat advection, soil moisture, and snow albedo, help to reinforce and sustain the warm events but are not the predominant triggering. Our work demonstrates that radiation controls the first order of temperature extremes and the Tibetan Plateau might face more risk of warm nights and compound warm events in the future.

1 Introduction

In recent years, increasing trends have been observed in the frequency, intensity, duration, and spatial extent of warm extremes (Seneviratne et al. 2014; Zhai and Pan 2003). These trends are projected to continue in the future (Sillmann et al. 2013; Thiery et al. 2021), with one of the most significant signals detected in the central and eastern Tibetan Plateau (Yin et al. 2019). Since extreme events have profound influences on human life, economic cost, agriculture, ecosystems, and hydrology (Easterling et al. 2000; UNDRR 2022), understanding the underlying mechanism is important to better forecast temperature extremes and reduce their detrimental impacts.

Previous studies have found that temperature extremes are accompanied by distinct large-scale circulation patterns, such as northern hemisphere heat extremes and amplified disturbances in the jet stream (Kornhuber et al. 2020; Mann et al. 2018), cold spells or heatwaves in Europe and the North Atlantic Oscillation (Guirguis et al. 2011; Scaife et al. 2008), and winter temperature extremes in China and the Arctic Oscillation (Ding et al. 2018; You et al. 2013). These linkages have previously been attributed to heat advection (Schumacher et al. 2019; Zhou and Yuan 2022) and local land-atmosphere interactions (Fischer et al. 2007; Miralles et al. 2014). Here, our goal is to evaluate extreme temperatures from a surface energy balance perspective (e.g., Lu and Cai 2009; Lesins et al. 2012; Gong et al. 2017; Lee et al. 2017; Sato and Simmonds 2021) to show that these are mostly caused by anomalies in the radiative forcing. We link extremes to anomalous surface energy components, and relate these to anomalies in the atmospheric circulation. With this, we aim to better identify the main causes of the occurrence of extreme temperatures.

To do so, we look at deviations of the climatological mean surface energy balance during the occurrence of temperature extremes. These perturbations relate to anomalies in net shortwave radiation (R_s), downward longwave radiation (R_{ld}), surface turbulent fluxes (J), and residuals (Q, mostly due to changes in ground heat fluxes) (Lee et al. 2017; Lesins et al. 2012). While R_s is generally related to variations in cloud cover and snow albedo, R_{ld} is largely determined by cloud cover, atmospheric water vapor, and near-surface air temperature, as reflected in semi-empirical parameterizations (Brutsaert 1975; Crawford and Duchon 1999). As for the sensible and latent heat fluxes, their sum (J) tends to self-adapt as

they are mostly constrained by the radiative forcing and thermodynamics (Kleidon 2014), while their partitioning is related to the soil moisture availability (Mueller and Seneviratne 2012). Compared with other terms, the magnitude of Q is much less on the Tibetan Plateau (Su et al. 2017). What this then means is that temperature anomalies are dominated by changes in radiation, which are mostly affected by changes in cloud cover. Furthermore, daily maximum temperatures relate primarily to the magnitude of solar radiation, while daily minimum temperatures to longwave radiation (Panwar et al. 2019). We can thus hypothesize that extremes in maximum temperature are primarily related to changes in solar radiation, while minimum temperatures primarily to longwave radiation. As both are modulated by cloud cover, we further hypothesize that the role of the large-scale circulation in the occurrence of extreme events primarily relates to changes in cloud cover.

We test our hypothesis by evaluating temperature extremes of the eastern Tibetan Plateau during the years from 1979 to 2018, using station data (National Meteorological Information Center, 2019) and station-based data (Fang et al. 2022, Fang and Mao 2022), as well as the ERA-5 reanalysis (Hersbach et al. 2018). We first identified temperature extremes as those outside the 5% - 95% range and calculated the anomalies in the surface energy balance during these periods. Then, the driver is further investigated by separating the effects on downward longwave radiation using a semi-empirical parameterization (Brutsaert 1975; Crawford and Duchon 1999) into contributions from atmospheric effective emissivity (cloud cover fraction and specific humidity) and air temperature. Since solar radiation has a strong diurnal variation, which significantly influences the diurnal range of turbulent heat fluxes, the main causes for extremely warm days and nights are likely to be different. We then relate these differences in radiation to the specific synoptic setting. Anticyclones are generally characterized by the absence of clouds, which favors the penetration of solar radiation during daytime and is likely to cause positive anomalies of maximum temperature, while cyclones are usually accompanied by more clouds and inhibit radiative cooling at night, thus possibly increasing the minimum temperature. To relate the occurrence due to these synoptic conditions, we thus distinguish between three kinds of warm extremes: independent warm day extremes (IWD), independent warm night extremes (IWN), and compound warm extremes (CW) that show extremes for both maximum and minimum temperatures. We also analyzed cold extremes to check the generality of our interpretation, but focus the main text only on the warm extremes during the winter (the additional analyses are provided as Supplementary Information).

This paper is organized as follows: Section 2 describes how extremes in surface temperature are identified and formulate our approach to estimating temperature deviations from anomalies in surface energy balance components. In the results section, we first present the anomalies in the surface energy balance and then relate them to the synoptic changes before and after the occurrence of the extremes. We then discuss potential limitations of our methodology, relate our findings to our hypothesis that extreme temperatures of the eastern Tibetan

plateau are caused mostly by the effect that circulation anomalies have on the radiative forcing, and describe some broader implications that follows from this hypothesis. We close with a brief summary and conclusions.

2 Data and Methods

2.1 Identification of temperature extremes

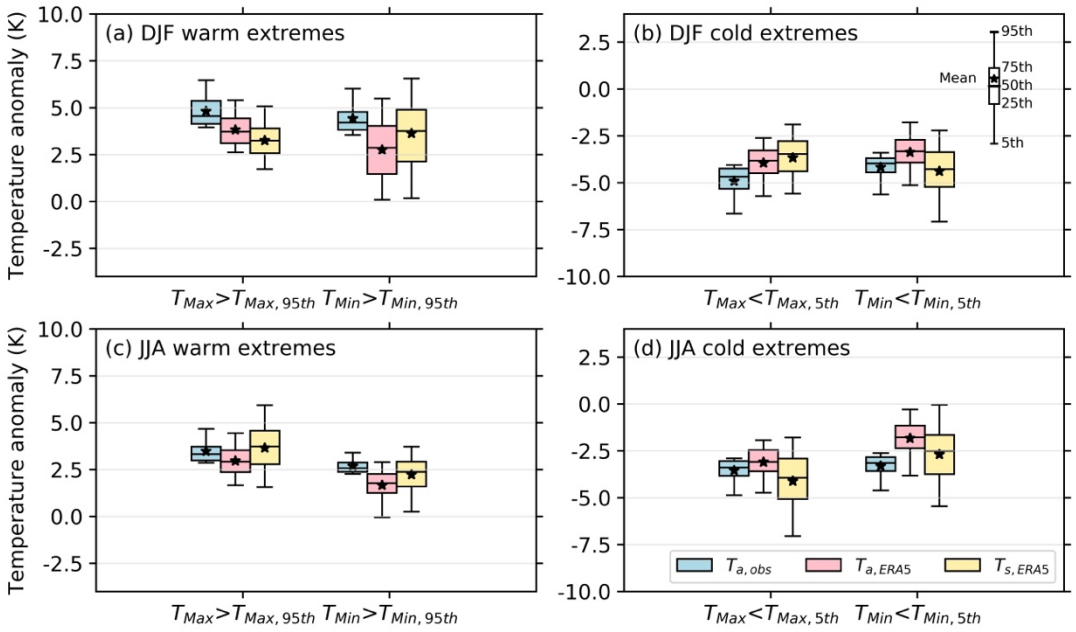

Figure 1. Temperature anomalies during (a, c) extremely warm days ($T_{\mathrm{Max}} > T_{Max,\ 95th}$) and nights ($T_{\mathrm{Min}} > T_{Min,\ 95th}$) and (b, d) extremely cold days ($T_{\mathrm{Max}} < T_{Max,\ 5th}$) and nights ($T_{\mathrm{Min}} < T_{Min,\ 5th}$) in observed air temperatures ($T_{a,obs}$), air temperatures from ERA5 ($T_{a,ERA5}$), and the surface skin temperature derived from ERA5 ($T_{s,ERA5}$) for (a, b) winter and (c, d) summer seasons. The box plots show the range of the regional-mean anomalies obtained from daily data.

We focus our analysis on the eastern Tibetan Plateau (ETP, 90°E~103E°, 27N°~40N°), which has a large number of weather stations (73 stations), while the western part has only 13 stations. To select the temperature extremes, the observed maximum and minimum 2m air temperatures (T_{Max} and T_{Min}) data (National Meteorological Information Center, 2019, for the period 1979-2010; Fang et al. 2022, for the period 2010-2018) during winter (DJF, December, January, and February) and summer (JJA, June, July, and August) spanning

from 1979 to 2018 was used. For station data (National Meteorological Information Center, 2019), data quality control and the homogeneity adjustment were performed using RclimDex (Zhang and Yang, 2004) and RHtestsV3 software packages (Wang and Feng, 2010), respectively. To evaluate the consistency of our analysis, we repeated our analysis looking at cold extremes, which we present in the Supplemental Information.

Warm extremes were identified based on the following four steps:

1. The seasonal cycle was removed by subtracting the multi-year average for every calendar day, and then the annual trend is removed by subtracting monthly-mean T_{Max} (also for T_{Min}) for each year from daily observations. This was done to avoid the identification of warm extremes at the end of February or at the end of the whole series only due to background climate or trends, when the thermodynamical or dynamical conditions nevertheless do not favor extreme temperatures.

2. Warm extremes for day and night were selected as those days at which regional-mean $T_{\mathrm{Max}} > T_{Max,\ 95th}$ for daytime extremes and $T_{\mathrm{Min}} > T_{Min,\ 95th}$ for nighttime extremes. The region-mean anomalies derived in this way are shown in Fig. 1.

3. Consecutive extreme warm days or nights were merged to get warm day (WD) and warm night (WN) events while keeping at least 3-days separation between every two events. More than 95% of the extreme warm events last no more than 3 days (Table S1).

4. Extreme warm events were divided into three kinds: 1) independent extreme warm days (IWD), when no WN event occurs within 24 hours before or after a WD event, 2) independent extreme warm nights (IWN), when no WD event occurs within 24 hours before or after a WN event, and 3) compound extreme warm events (CW) when WN and WD events occur simultaneously in no more than 24 hours apart from each other. The frequency and the temperature evolution are shown in Table S1 and Fig S1, respectively. Since warm days precede warm nights in more than 90% of the CW events, the other case in which compound events started with a warm night are excluded in this work.

We repeated this analysis using hourly data from ERA5 (Hersbach et al. 2018) of air temperature ($T_{a,ERA5}$) and surface skin temperature ($T_{s,ERA5}$), using the same dates at which the extremes occurred in the observations (selecting the maximum and minimum based on hourly data with interval as 1 hour). This was done to check how adequate the use of ERA5 is to identify the cause of extreme temperatures. As shown in Fig. 1, when extremes are observed in $T_{a,obs}$, anomalies in $T_{a,ERA5}$ and $T_{s,ERA5}$ reach a comparable level. This justifies the use of ERA5 data and surface energy balance anomalies to understand the causes of extreme temperatures on the eastern Tibetan plateau.

2.2 Decomposition of changes in surface temperature

To attribute the temperature extremes to anomalies in the surface energy balance, we first write the energy balance as,

$$\mathbf{R}_{\mathrm{ld}} - \mathbf{R}_{\mathrm{lu}} + \mathbf{R}_{\mathbf{s}} - \mathbf{J} = \mathbf{Q}, \quad (2.1)$$

where R_{ld} is the downward flux of longwave radiation, R_{lu} the emitted upward flux of longwave radiation, R_s the net absorption of solar radiation, J the turbulent heat flux, and Q the ground heat flux. Note that the radiation terms are downward positive and turbulent heat flux is upward positive. By using $\sigma {T_s}^4$ for R_{lu} (with σ being the Stefan-Boltzmann constant and T_s the surface temperature), we can express an anomaly T_s as,

$$\mathbf{T_s} = (\mathbf{R}_{\mathrm{ld}} + \mathbf{R_s} - \mathbf{J} - \mathbf{Q}) / \mathbf{4}\,\overline{\mathbf{T_s}}^{\mathbf{3}}, \quad (2.2)$$

where the right-hand side includes the anomalies of the surface energy balance components. In this way, changes in the surface temperature can be attributed to the four components represented by terms on the right-hand of Equation 2.2.

To perform the decomposition, hourly data from ERA5 for $T_{s,ERA5}$, R_{ld}, R_s, and J are used, and Q is obtained as the residual from the balance. To determine the driving factors of the anomaly in R_{ld}, we express it using the semi-empirical expression from Brutsaert (1975) and Crawford and Duchon (1999). They express R_{ld} as

$$\mathbf{R}_{\mathrm{ld}} = \mathbf{T_a}^{\mathbf{4}}, \quad (2.3)$$

where ε is the emissivity and T_a the near-surface air temperature. We can then express an anomaly R_{ld} as

$$\mathbf{R}_{\mathrm{ld}} = \overline{\mathbf{T_a}}^{\mathbf{4}} + \mathbf{4}\,\overline{\mathbf{T_a}}^{\mathbf{3}}\,\mathbf{T_a}\,, \quad (2.4)$$

and attribute these to either variations in emissivity ($R_{ld,\varepsilon}$) or temperature ($R_{ld,T}$), which are the first and second term at the right hand of Eq. 2.4, respectively. The emissivity is related to cloud fraction f_c and water vapor pressure e_a as in (Brutsaert 1975; Crawford and Duchon 1999):

$$= \mathbf{f_c} + (\mathbf{1} - \mathbf{f_c})\left(\mathbf{1.24}\left(\frac{\mathbf{e_a}}{\mathbf{T_a}}\right)^{\frac{1}{7}}\right). \quad (2.5)$$

We can thus further decompose changes in emissivity into contributions by cloud fraction (ε_{f_c}) or atmospheric humidity (ε_{e_a}) (corresponding to the first and second term at the right hand of Eq. 2.6, respectively; the term related to T_a is relatively small in magnitude, thus is ignored here):

$$\approx (\mathbf{1}-\mathbf{1.24}\left(\frac{\mathbf{e_a}}{\mathbf{T_a}}\right)^{\frac{\mathbf{1}}{\mathbf{7}}})\ \mathbf{f_c}+\frac{\mathbf{1.24}}{\mathbf{7}}\frac{(\mathbf{1}-\overline{\mathbf{f_c}})}{(\overline{\mathbf{e_a}})^{\mathbf{6/7}}(\overline{\mathbf{T_a}})^{\mathbf{1/7}}}\ \underset{\mathbf{a}}{\mathbf{e}}\ . \quad (2.6)$$

We used total cloud cover (TCC) and dew point temperature from ERA5 to calculate these parameters. Cloud cover was also applied to analyze the changes in solar radiation.

3 Results

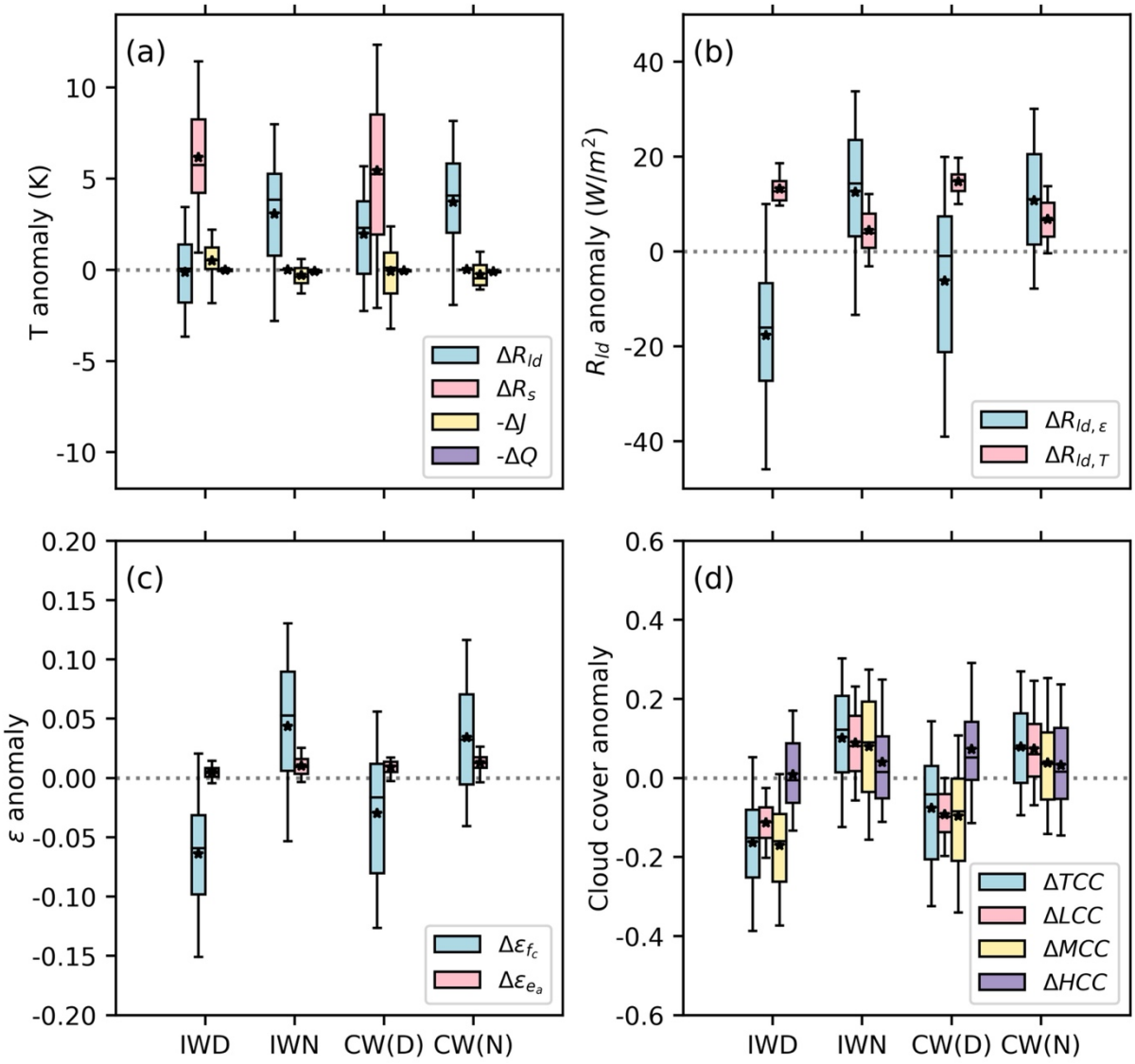

Figure 2. Decomposition of surface temperature anomalies during warm temperature extremes during winter (IWD = Independent Warm Days; IWN = Independent Warm Nights; CW: Compound events during (D) days and (N) nights). The average and spread among events of (a) regional-mean anomalies of surface temperature due to changes in the downward longwave radiation (R_{ld}), net solar radiation (R_s), surface turbulent heat flux ($-J$), and ground heat flux ($-Q$) (cf. Eq. 2.2); (b) regional-mean anomalies of R_{ld} due to changes in emissivity ($R_{ld,\varepsilon}$) and near-surface air temperature ($R_{ld,T}$) using Brutsaert's

(1975) parameterization (cf. Eq. 2.4); (c) regional-mean anomalies of emissivity due to changes in cloud cover change (ε_{f_c}) and water vapor pressure (ε_{e_a}) using Crawford and Duchon's (1999) parameterization (cf. Eq. 2.6); and (d) regional-mean anomalies of total, low-level, medium-level, and high-level cloud cover fraction (TCC, LCC, MCC, and HCC).

3.1 Decomposition of temperature and longwave radiation

Fig. 2a shows the decomposition of the anomalies in surface temperature during warm extreme events in winter. Independent extreme events during the day are caused by increases in solar radiation (R_s), while nighttime extremes are dominated by increases in downwelling longwave radiation (R_{ld}). A positive change in turbulent heat fluxes (J) does not appear to take place during daytime extremes, hence playing no role in shaping the temperature extreme. As for the compound events, its daytime witnesses both positive anomalies in shortwave and longwave radiation, with the former approximately twice as high as the latter, while its nighttime condition resembles the setting during the independent warm night events.

Considering that it is primarily the anomalies in radiation that shape temperature extremes in winter, the causes for these anomalies are further analyzed in Figs. 2b-2d. During all warm extremes (Fig. 2b), increases in air temperature contribute to the increase in downward longwave radiation ($R_{ld,T}$), with a larger value during warm days than nights due to the higher sensitivity ($4\sigma\bar{\varepsilon}\overline{T_a}^3$). Due to changes in emissivity ($R_{ld,\varepsilon}$), this positive anomaly is offset during daytime while enhanced during nighttime. This anomaly is mostly caused by variations in cloud cover (ε_{f_c}), especially the low- and medium- level clouds (Fig. 2d), although moisture anomalies (ε_{e_a}) add to these changes to a limited extend during all warm extremes (Fig. 2c). Decreases in cloud cover during warm days also explain the enhanced solar radiation.

3.2 Drivers of cloud variation

Since cloud cover variations play the dominant role in modulating radiation arriving at the surface during warm extremes during day and night, we next linked these to anomalies in the atmospheric circulation. To do so, we evaluated anomalies in the vertical motion of air, the horizontal convergence of clouds, and the related large-scale circulation pattern, as averages (Fig. 3) and as spatial fields (Fig. 4). Figs. 3 and 4 present results related to events of one-day length because they account for most of the extreme events (Tables S1-S4), but longer events show similar patterns (not shown). The independent warm daytime extreme events are preceded by a persistent anticyclone (Fig. 4), which favors the sinking of air particles (Fig. 3a), and suppresses the formation of clouds (Figs. 2d, 3b), thus increasing the atmospheric transmittance and allows more solar radiation to penetrate and reach the ground (Fig. 2a, 3c). Although the convergence of liquid and frozen clouds is also reduced (Figs. 3e and 3f), the anomalies are not significant, meaning that the subsidence of air is the dominant cause of the cloud reduction. On the contrary, the independent warm

night extreme events are controlled by a low-pressure system and upward motion, which enhance cloud cover and atmospheric emissivity. These events also experience a significantly amplified convergence of cloud liquid or frozen water, which further adds to the increase in downward longwave radiation. Different from independent warm extreme events, compound events witness an equatorward Rossby wave which originates from the Arctic and passes through the Eurasian continent. The propagation of this Rossby wave leads to a quick shift from high-pressure to a low-pressure system over the eastern Tibetan plateau, which not only favors the sinking of air and clear-sky conditions during daytime of compound extreme events, but also brings in more convergence of cloud frozen water flux over the region in the following night, therefore strengthening the magnitude and extension of the warm extreme event. This emphasizes the importance of changes in cloud cover in extreme warm events over the eastern Tibetan Plateau and establishes a mechanistic link to anomalies in the circulation.

The mechanism described above also explains most parts of the warm events during summer (Figs. S2-S3), which have three slight differences compared to the winter events: first, the contribution of solar radiation (R_s) to extremely warm days is relatively larger; second, the effect of cloud increase on emitting more longwave radiation downward (ε_{f_c}) during warm nights is weaker (which can be attributed to $(1 - 1.24\left(\frac{e_a}{T_a}\right)^{\frac{1}{7}})$ being less in the moister summer); and third, the anomalies in the horizontal convergence of cloud water have little significance during summer warm extreme events. The cold extreme events have generally the opposite anomalies of their corresponding warm events (Fig. S4-S7), thus further supporting our interpretation. It would thus seem that extreme temperature events of the eastern Tibetan plateau are primarily shaped by radiation anomalies that are linked to anomalies in circulation, which cause changes in cloud cover, but not because of changes in heat advection.

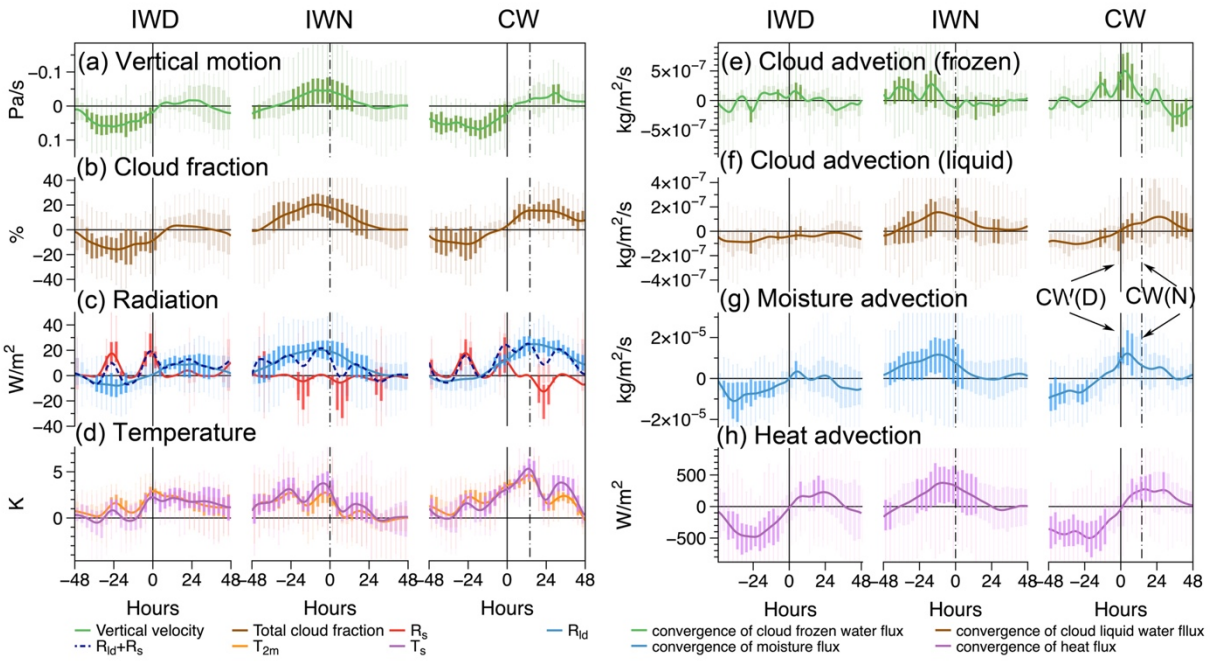

Figure 3. Temporal evolution of anomalies in (a) vertical velocity (downward positive), (b) cloud cover fraction, (c) shortwave and longwave radiation, (d) the surface and air temperature, (e) cloud frozen water advection, (f) cloud liquid water advection, (g) moisture advection, and (h) heat advection for independent warm day events (IWD), independent warm night events (IWN), and the compound warm events (CW) in winter. Advection means vertically integrated convergence of flux. Vertical solid and dashed lines mark the extreme warm day and night events, respectively. The box plot shows the mean value and ranges among events, with the upper and lower whistles presenting 95^{th} and 5^{th}, the upper and lower edge of the box presenting 75^{th} and 25^{th}. Heavy lines are Loess fit lines. Heavy color boxes present the value with statistical significance at the 95% confidence level based on a two-sample student's t-test.

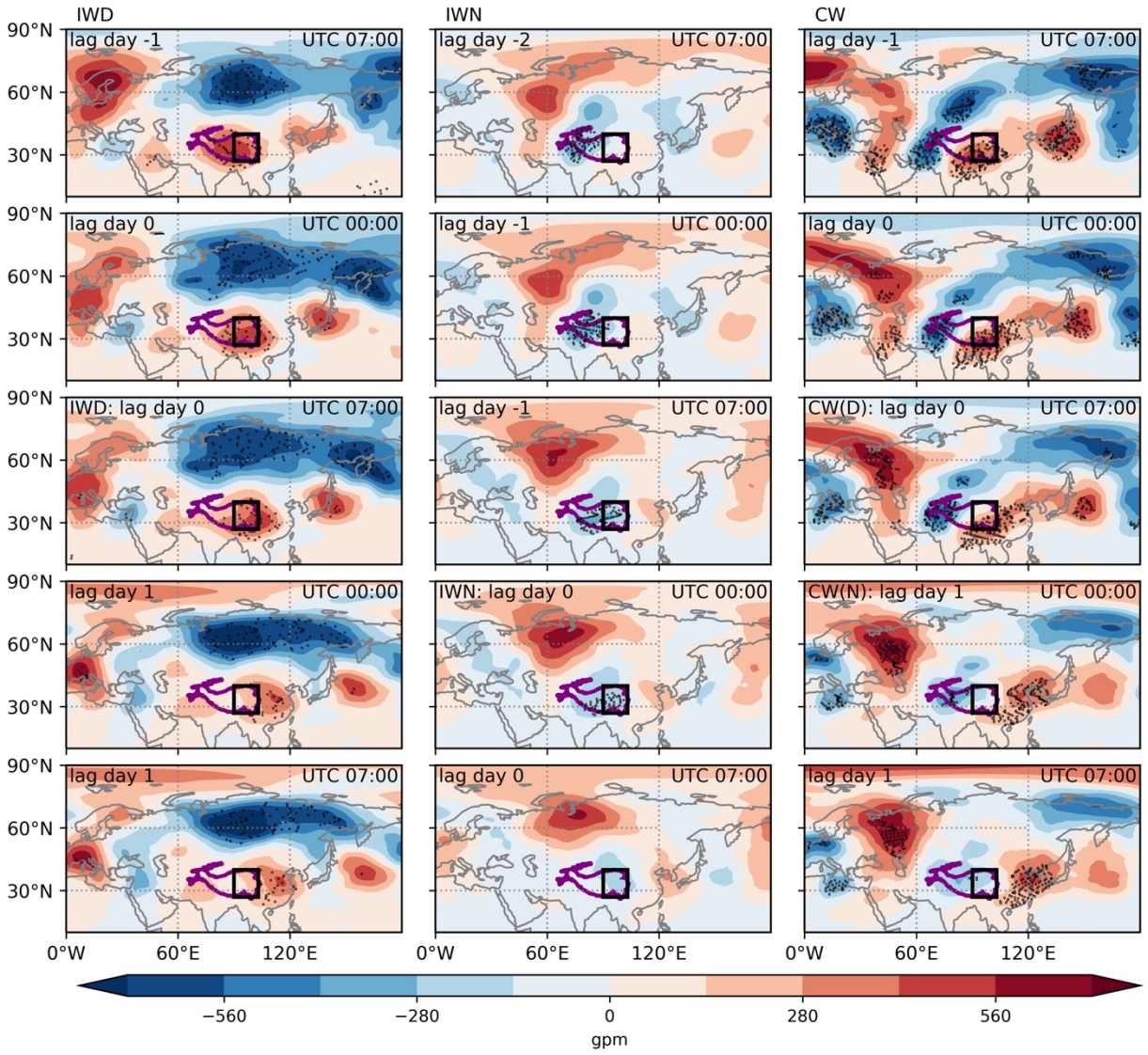

Figure 4. The evolution of geopotential height anomalies on 500 hPa before and after independent warm extreme events (IWD, the first column), independent warm night extremes (IWN, the second column), and compound events (CW, third column). Shading presents the anomalies of geopotential height, with the dots indicating values statistically significant at the 95% confidence level. The anomalies of geopotential height are plotted from 24 hours (the first row) before to 24 hours after (the last row) the IWD and CW events are triggered, while from 41 hours (the first row) before to 7 hours after (the last row) the IWN events. According to ERA5 hourly data, daily T_{max} and T_{min} over the winter Tibetan

Plateau generally occur around UTC 07:00 and UTC 00:00, respectively.

4 Discussion

4.1 Limitations

One of our most important assumptions is that the variation of the surface, or skin temperature (T_s) can explain that of near-surface air temperature (T_a). However, in winter (Fig. 1a), it can be seen that anomalies of T_a are higher than those of T_s during extremely warm days but lower during nights. This bias might be related to changes in boundary layer height (BLH) because the daytime energy input contributes to increases in both T_a and BLH simultaneously (Panwar et al. 2019). During warm extremes during the day, the growth of the boundary layer may be suppressed by air subsidence (as shown in Fig. 3a), which may result in an amplified increase of T_a that may not be reflected in T_s. During warm nights, however, the greater presence of clouds may have a stronger effect of reducing surface cooling than atmospheric cooling with a weaker nighttime inversion, so that the response in T_s would be greater than that in T_a. Although there is a slight disparity, most of the air temperature anomalies during extremes can be explained very well by anomalies of the surface energy balance, resulting in similar magnitudes and evolution of anomalies in T_a and T_s (Figs. 1 and 3d). This is consistent with findings in previous studies (Lee et al. 2017), so this bias does not seem to affect our interpretation.

4.2 Role of heat advection, land-atmosphere interactions, and adiabatic heating

While we focus here on the role of cloud anomalies and their effects on radiative fluxes, previous studies attributed extreme events to anomalies in heat advection, sensible heat flux, and adiabatic heating (Fischer et al. 2007; Li et al. 2021; Schumacher et al. 2019). By increasing air temperature, T_a, these suggested alternatives would result in surface warming by enhancing the downwelling longwave radiation through the contribution $R_{ld,T}$ (Eqs 2.2 and 2.4), but not by changing the emissivity, ε, which results in the contribution $R_{ld,\varepsilon}$. Our results show that $R_{ld,\varepsilon}$ contributes more than twice to the enhancement of R_{ld} than $R_{ld,T}$ (Figs. 2b and 2c). This implies that the warming at night over the eastern Tibetan plateau originates primarily due to a cloud cover change, and not due to the suggested alternatives. In addition, as is shown by the horizontal convergence of temperature (multiplied by specific heat capacity) and moisture fluxes in Figs. 3g and 3h, heat advection into the eastern Tibetan plateau only increases significantly during extremely warm nights but decreases on extremely warm days. This can be explained by the presence of the high-pressure system and the associated subsiding motion (Figs. 3a and 4). No significant changes in the sensible heat flux were found, excluding this as an alternative explanation (Fig. S8f). Therefore, our interpretation of the dominant effect of cloud cover changes in shaping extreme temperatures of the eastern Tibetan plateau appears to best explain our findings.

Here, we have only evaluated the triggering of extreme temperature events.

This raises the question of how our findings relate to the mechanisms involved in developing heat waves. Previous studies have found that the mechanism for heat waves in Eastern Asia might vary with their life stages (Seo et al. 2021). Hence, we repeated our analysis with a longer time window of events lasting at least three days over the eastern Tibetan plateau and evaluated the contributions to changes in downward longwave radiation (Fig. S8). We find that 48 hours after the onset of such a longer-lasting extreme event, the positive anomalies of R_{ld} start to reach that of R_s (Fig. S8c), with the partial contribution of warmer air temperature ($R_{ld,T}$) comparable to that of cloud cover increase (R_{ld,f_c}) (Fig. S8e). Moreover, during this time, the sensible heat flux and heat advection are predominant in warming the atmosphere (Figs. S8f and S8g), which is consistent with previous studies (Miralles et al. 2014; Schumacher et al. 2019). The adiabatic heating is, however, negative because the anticyclone has already been shifted to the cyclone (Fig. 4), which is accompanied by ascending air (Fig. S8a). In addition, 24 hours after the onset of the longer-lasting event, a significant decrease in snow albedo is found because of the warmer surface (Figs. S8d and S8h), which leads to positive feedback by substantially enhancing the absorption of solar radiation during winter warm extremes (Fig. S8c). However, these reinforcements are not found during the summer season (Fig. S9). What this shows is that while we evaluated the main drivers for extreme temperature events of the eastern Tibetan plateau, there may be other factors playing a role when it comes to heat waves that may be specific to the region, can vary among seasons, with the relative contributions changing as a heat wave develops.

4.3 Implications

Our interpretation that anomalies in radiation are the main cause for temperature extremes has direct implications for expected trends with global warming. Observations show that nighttime temperatures respond more sensitively to an increase in the greenhouse effect than daytime temperatures, thereby reducing the diurnal temperature range (Easterling et al. 1997, Du et al. 2020). This effect can be explained by the buffering effect of the convective boundary layer and the strong diurnal variation of turbulent fluxes on land (Kleidon and Renner 2017). Our results are consistent with these observations and interpretation. In the compound events, the radiative forcing is around 20 W/m^2 during day and night (Fig. 3c), but the associated nighttime temperature anomaly is as high as 5 K while only 2.5 K during the daytime (Fig. 3d). This stronger temperature sensitivity at night can also be found during summer and for cold events (Figs. S3, S5, and S7). Since global warming is mostly associated with an increase in downward longwave radiation, we would expect that warm extremes at night become more frequent and intense than daytime extremes.

In addition to the difference between extremely warm days and nights, our results imply that the future trend of independent and compound events might also differ. In Fig. 4, only the compound warm events in winter are preceded by an equatorward Rossby wave from the Arctic, which is possibly triggered by the sea ice retreat in the Arctic (Duan et al. 2022). This suggests an increase in

both frequency and severity of such Rossby wave events and thus such compound warm events in winter Tibetan Plateau due to the significant negative trend of the Arctic sea ice extent (Overland and Wang 2013; Simmonds 2015).

5 Summary and Conclusions

We analyzed temperature extreme events of the eastern Tibetan plateau and attributed these events to anomalies in the surface energy balance. We found that extremely warm days are caused by greater solar radiation warming because of less cloud cover that is associated with large-scale subsidence controlled by a persistent high-pressure system. Extremely warm nights are mainly caused by increases in downward longwave radiation due to clouds related to the presence of a low-pressure system. Compound events were associated with an equatorward Rossby wave, which led to a change in the radiative conditions that favored both, extremely warm daytime and nighttime temperatures. Hence, in all cases, the direct cause for the extreme temperatures were radiation anomalies that were caused by cloud cover changes associated with specific synoptic conditions. We conclude that the atmospheric circulation affected temperature extremes of the eastern Tibetan plateau primarily by changing cloud cover, but not by horizontal heat advection. The extent to which this interpretation holds more generally also in other regions would need to be explored in further research.

Acknowledgments, Samples, and Data

This research was supported by the Second Tibetan Plateau Scientific Expedition and Research Program (grant no. 2019QZKK0208), National Key Research and Development Program of China (grant no. 2016YFE0201900), and the National Natural Science Foundation of China (grant no. 91547204).

Data presented in this manuscript are available through the National Tibetan Plateau Data Center (TPDC, http://data.tpdc.ac.cn/en/) and the Copernicus Climate Chang Service Climate Data Store (CDS, https://doi.org/10.24381/cds.adbb2d47 and https://doi.org/10.24381/cds.bd0915c6).

References

Brutsaert, W., 1975: On a derivable formula for long-wave radiation from clear skies. *Water Resources Research*, **11,** 742-744.

Crawford, T. M., and C. E. Duchon, 1999: An Improved Parameterization for Estimating Effective Atmospheric Emissivity for Use in Calculating Daytime Downwelling Longwave Radiation. *Journal of Applied Meteorology*, **38,** 474-480.

Ding, Z., Y. Wang, and R. Lu, 2018: An analysis of changes in temperature extremes in the Three River Headwaters region of the Tibetan Plateau during 1961–2016. *Atmospheric Research*, **209,** 103-114.

Duan, A., and Coauthors, 2022: Sea ice loss of the Barents-Kara Sea enhances the winter warming over the Tibetan Plateau. *npj Climate and Atmospheric Science*, **5,** 26.

Easterling, D. R., J. L. Evans, P. Y. Groisman, T. R. Karl, K. E. Kunkel, and P. Ambenje, 2000: Observed Variability and Trends in Extreme Climate Events: A Brief Review. *Bulletin of the American Meteorological Society*, **81,** 417-426.

Easterling, D. R., and Coauthors, 1997: Maximum and Minimum Temperature Trends for the Globe. *Science*, **277,** 364-367.

Fang, S., Mao, K. 2022. A dataset of daily near-surface air temperature in China from 1979 to 2018. National Tibetan Plateau Data Center, DOI: 10.5281/zenodo.5502275. (Accessed on < 06-03-2022 >)

Fang, S., Kebiao Mao, Xia, X., Wang, P., Shi, J., Bateni, S. M., Xu, T., Cao, M., and Heggy, E. Qin. Z., 2022. Dataset of daily near-surface air temperature in China from 1979 to 2018. Earth Syst. Sci. Data, 14, 1-20, 2022. https://essd.copernicus.org/articles/14/1413/2022/

Fischer, E. M., S. I. Seneviratne, D. Lüthi, and C. Schär, 2007: Contribution of land-atmosphere coupling to recent European summer heat waves. *Geophysical Research Letters*, **34**.

Guirguis, K., A. Gershunov, R. Schwartz, and S. Bennett, 2011: Recent warm and cold daily winter temperature extremes in the Northern Hemisphere. *Geophysical Research Letters*, **38**.

Hersbach, H., and Coauthors, 2018: ERA5 hourly data on single levels from 1959 to present. Copernicus Climate Change Service (C3S) Climate Data Store (CDS). (Accessed on < 06-03-2022 >), 10.24381/cds.adbb2d47

Kleidon, A., M. Renner, and P. Porada, 2014: Estimates of the climatological land surface energy and water balance derived from maximum convective power. *Hydrol. Earth Syst. Sci.*, **18,** 2201-2218.

Kleidon, A., and M. Renner, 2017: An explanation for the different climate sensitivities of land and ocean surfaces based on the diurnal cycle. *Earth Syst. Dynam.*, **8,** 849-864.

Kornhuber, K., D. Coumou, E. Vogel, C. Lesk, J. F. Donges, J. Lehmann, and R. M. Horton, 2020: Amplified Rossby waves enhance risk of concurrent heatwaves in major breadbasket regions. *Nature Climate Change*, **10,** 48-53.

Lee, S., T. Gong, S. B. Feldstein, J. A. Screen, and I. Simmonds, 2017: Revisiting the Cause of the 1989–2009 Arctic Surface Warming Using the Surface Energy Budget: Downward Infrared Radiation Dominates the Surface Fluxes. *Geophysical Research Letters*, **44,** 10,654-610,661.

Lesins, G., T. J. Duck, and J. R. Drummond, 2012: Surface Energy Balance Framework for Arctic Amplification of Climate Change. *Journal of Climate*, **25,** 8277-8288.

Li, Y., Y. Ding, and Y. Liu, 2021: Mechanisms for regional compound hot extremes in the mid-lower reaches of the Yangtze River. *International Journal of Climatology*, **41,** 1292-1304.

Mann, M. E., S. Rahmstorf, K. Kornhuber, B. A. Steinman, S. K. Miller, S. Petri, and D. Coumou, 2018: Projected changes in persistent extreme summer weather events: The role of quasi-resonant amplification. *Science Advances*, **4,** eaat3272.

Miralles, D. G., A. J. Teuling, C. C. van Heerwaarden, and J. Vilà-Guerau de Arellano, 2014: Mega-heatwave temperatures due to combined soil desiccation and atmospheric heat accumulation. *Nature Geoscience*, **7,** 345-349.

Mueller, B., and S. I. Seneviratne, 2012: Hot days induced by precipitation deficits at the global scale. *Proceedings of the National Academy of Sciences*, **109,** 12398-12403.

National Meteorological Information Center, 2019: Daily meteorological dataset of basic meteorological elements of China National Surface Weather Station (V3.0) (1951-2010). National Tibetan Plateau Data Center. (Accessed on < 06-03-2022 >)

Overland, J. E., and M. Y. Wang, 2013: When will the summer Arctic be nearly sea ice free? *Geophysical Research Letters*, **40,** 2097-2101.

Panwar, A., A. Kleidon, and M. Renner, 2019: Do Surface and Air Temperatures Contain Similar Imprints of Evaporative Conditions? *Geophysical Research Letters*, **46,** 3802-3809.

Scaife, A. A., C. K. Folland, L. V. Alexander, A. Moberg, and J. R. Knight, 2008: European Climate Extremes and the North Atlantic Oscillation. *Journal of Climate*, **21,** 72-83.

Schumacher, D. L., J. Keune, C. C. van Heerwaarden, J. Vilà-Guerau de Arellano, A. J. Teuling, and D. G. Miralles, 2019: Amplification of mega-heatwaves through heat torrents fuelled by upwind drought. *Nature Geoscience*, **12,** 712-717.

Seneviratne, S. I., M. G. Donat, B. Mueller, and L. V. Alexander, 2014: No pause in the increase of hot temperature extremes. *Nature Climate Change*, **4,** 161-163.

Seo, Y.-W., K.-J. Ha, and T.-W. Park, 2021: Feedback attribution to dry heatwaves over East Asia. *Environmental Research Letters*, **16,** 064003.

Sillmann, J., V. V. Kharin, F. W. Zwiers, X. Zhang, and D. Bronaugh, 2013: Climate extremes indices in the CMIP5 multimodel ensemble: Part 2. Future climate projections. *Journal of Geophysical Research: Atmospheres*, **118,** 2473-2493.

Simmonds, I., 2015: Comparing and contrasting the behaviour of Arctic and Antarctic sea ice over the 35 year period 1979-2013. *Annals of Glaciology*, **56,** 18-28.

Su, J., A. Duan, and H. Xu, 2017: Quantitative analysis of surface warming amplification over the Tibetan Plateau after the late 1990s using surface energy

balance equation. *Atmospheric Science Letters*, **18,** 112-117.

Thiery, W., and Coauthors, 2021: Intergenerational inequities in exposure to climate extremes. *Science*, **374,** 158-160.

UNDRR, U. N. O. f. D. R. R., 2022: Heatwaves: Addressing a sweltering risk in Asia-Pacific, 37 p. pp.

Yin, H., Y. Sun, and M. G. Donat, 2019: Changes in temperature extremes on the Tibetan Plateau and their attribution. *Environmental Research Letters*, **14,** 124015.

You, Q., G. Ren, K. Fraedrich, S. Kang, Y. Ren, and P. Wang, 2013: Winter temperature extremes in China and their possible causes. *International Journal of Climatology*, **33,** 1444-1455.

Zhai, P., and X. Pan, 2003: Trends in temperature extremes during 1951–1999 in China. *Geophysical Research Letters*, **30**.

Zhou, S., and X. Yuan, 2022: Upwind Droughts Enhance Half of the Heatwaves Over North China. *Geophysical Research Letters*, **49,** e2021GL096639.

Wang, X. L., and Y. Feng (2010), RHtestsV3 User Manual, UserManual.doc. *Climate Research Division, Science and Technology Branch, Environment Canada*, Toronto, Ontario, Canada. 26 pp. Available online at http://cccma.seos.uvic.ca/ETCCDMI/RHtest/RHtestsV3.

Zhang, X., & Yang, F. (2004). RClimDex (1.0) user manual. *Climate Research Branch Environment Canada*, *22*. http://etccdi.pacificclimate.org/software.shtml